

The optimal redshift for detecting ionized bubbles in HI 21-cm maps

Kanan K. Datta^{1*}, Somnath Bharadwaj^{1†} and T. Roy Choudhury^{2‡}

¹*Department of Physics and Meteorology & Centre for Theoretical Studies, IIT, Kharagpur 721302, India*

²*Harish-Chandra Research Institute, Chhatmag Road, Jhusi, Allahabad 211019, India*

28 October 2018

ABSTRACT

The detection of individual ionized bubbles in HI 21-cm maps is one of the most promising, direct probes of the epoch of reionization (EoR). At least 1000 hrs of observation would be required for such a detection with either the currently functioning GMRT or the upcoming MWA. Considering the large investment of telescope time it is essential to identify the “optimal redshift” where the prospects of a detection are most favourable. We find that the optimal redshift is determined by a combination of instrument dependent factors and the evolution of the neutral fraction x_{HI} . We find that the redshift range 8.1 ± 1.1 and 9.8 ± 1 are optimum for detecting ionized bubbles with the GMRT and MWA respectively. The prospects of a detection, we find, are more favourable in a scenario with late reionization with $x_{\text{HI}} \approx 0.5$ at $z \approx 7.5$ as compared to an early reionization model where $x_{\text{HI}} \approx 0.5$ at $z \approx 10$. In the late reionization scenario, for both instruments a 3σ detection is possible for bubbles of comoving radius $R_b \geq 30$ Mpc with 1000 hrs of observation. Future observations will either lead to the detection of ionized bubbles, or in the event of non-detection, lead to constraints on the product $x_{\text{HI}} R_b^\gamma$ for the observational volume, where $\gamma = 1.5$ and 2 for GMRT and MWA respectively.

Key words: cosmology: theory, cosmology: diffuse radiation, Methods: data analysis

1 INTRODUCTION

It is currently accepted that the Universe was reionized by the growth of ionized bubbles around luminous sources in the redshift range $z \sim 6 - 15$ (Fan et al. 2006; Choudhury & Ferrara 2006; Komatsu et al. 2008). Detection of individual ionized bubbles (HII regions) in HI 21-cm maps of reionization is one of the major, important approaches that will be adopted by the present and upcoming radio experiments (GMRT, MWA, LOFAR, SKA) to probe the EoR. Such observations will directly probe the properties of the ionizing sources and the evolution of the surrounding IGM (Wyithe & Loeb 2004; Wyithe, Loeb & Barnes 2005; Maselli et al. 2007; Geil & Wyithe 2007) and are expected to complement the study of reionization through the power spectrum of HI brightness temperature fluctuations. Detection of individual bubbles is a big challenge because the HI signal will be buried in strong foregrounds and system noise (Ali et al. 2008).

In an earlier paper (Datta, Bharadwaj & Choudhury 2007), hereafter referred to as Paper I, we have proposed a visibility based matched filter technique to optimally combine the entire HI signal from an ionized bubble while removing the foregrounds and minimizing system noise. Using visibilities has an advantage over image based techniques because the system noise contribution in

different visibilities is independent whereas the noise in different pixels of a radio-interferometric images is not. Our investigations show that for both the GMRT and the MWA, at redshift $z = 8.5$, it will be possible to detect ionized bubbles of comoving radius $R_b > 40$ Mpc and $R_b > 22$ Mpc in 100 and 1,000 hours of observations respectively. We also find that fluctuations in the HI outside the bubble that we are trying to detect impose a fundamental restrictions on the smallest bubble that can be detected. Assuming that the HI outside the bubble traces the dark matter, we find that it will not be possible to detect bubbles with comoving radius less than 8 and 16 Mpc with the GMRT and the MWA respectively, however large be the integration time. In a subsequent paper (Datta et al. 2008), hereafter referred to as Paper II) we have used simulations to validate our matched filter technique and assess the impact of patchy reionization outside the bubble that we are trying to detect on the bubble detection.

The question “What is the optimal redshift for bubble detection?” is particularly important when planning future observations. Estimates show (Papers I and II) that at least 1000 hrs of observation will be required for a detection with either the GMRT or the MWA. Considering the large investment in observing time, it is important to target the redshift where the prospect of a detection is most favourable. In addition, it is important to have a clear picture of the different factors that contribute towards deciding the most optimal redshift. We expect this to provide insights useful for the design of future observational programmes and also the design of future low-frequency radio telescopes.

* E-mail: kanan@phy.iitkgp.ernet.in

† E-mail: somnathb@iitkgp.ac.in

‡ E-mail: tirth@hri.res.in

A variety of redshift dependent factors influence the signal from an ionized bubble. While a number of these pertain to the instrument in question, the frequency dependence of the sky temperature and the redshift evolution of the neutral hydrogen fraction also play an important role. In this paper we analyze all of the effects that determine the optimal redshift for detecting ionized bubbles. We consider two different models for the redshift evolution of the neutral fraction and make predictions for the GMRT and the MWA.

The paper is organized as follows. In Section 2 we briefly review the matched filter technique for bubble detection. In Section 3 we establish scaling relations for the matched filter signal to noise ratio (SNR) assuming a uniform baseline distribution. We also discuss the models of HI evolution that we adopt. We present our results and conclusions in Section 4.

Throughout out this paper we adopt cosmological parameters from (Dunkley et al. 2009). For the GMRT we use the antenna specifications from their web site and for the MWA we use the instrumental parameters from (Bowman et al. 2007).

2 THE MATCHED FILTER TECHNIQUE FOR DETECTING IONIZED BUBBLES IN REDSHIFTED 21-CM MAPS

The visibility recorded in a radio-interferometric observation of an ionized bubble can be written as

$$V(\vec{U}, \nu) = S(\vec{U}, \nu) + HF(\vec{U}, \nu) + N(\vec{U}, \nu) + F(\vec{U}, \nu). \quad (1)$$

Here we refer to $\vec{U} = \mathbf{d}/\lambda$ as a baseline, \mathbf{d} being the physical separation between a pair of antennas projected on the plane perpendicular to the line of sight and λ is wavelength corresponding to the observed frequency ν . In eq. (1) $S(\vec{U}, \nu)$ is the HI signal from the ionized bubble, $HF(\vec{U}, \nu)$ is the contribution from fluctuations in the HI outside the target bubble, $N(\vec{U}, \nu)$ is the system noise and $F(\vec{U}, \nu)$ is the contribution from other astrophysical foregrounds. The contributions $HF(\vec{U}, \nu)$, $N(\vec{U}, \nu)$ and $F(\vec{U}, \nu)$ are all assumed to be random variables with zero mean, whereby $\langle V(\vec{U}, \nu) \rangle = \langle S(\vec{U}, \nu) \rangle$. The angular brackets here denote average with respect to different realizations of the HI fluctuations, system noise and foregrounds.

We consider a spherical ionized bubble of comoving radius R_b centered at redshift z_c located at the center of the field of view (FoV). The bubble is assumed to be embedded in an uniform IGM with neutral hydrogen fraction x_{HI} . A bubble of comoving radius R_b will be seen as a circular disc in each of the frequency channels that cut through the bubble. At a frequency channel ν , the angular radius of the disc is $\theta_\nu = (R_b/r_\nu)\sqrt{1 - (\Delta\nu/\Delta\nu_b)^2}$ where $\Delta\nu = \nu_c - \nu$ is the distance from the bubble's center $\nu_c = 1420 \text{ MHz}/(1 + z_c)$ and $\Delta\nu_b = R_b/r'_\nu$ is the bubble's radius in frequency space. Here r_ν is the comoving distance corresponding to $z = (1420 \text{ MHz}/\nu) - 1$, and $r'_\nu = dr_\nu/d\nu$. The expected visibility signal $S(\vec{U}, \nu)$ in each frequency channel is the Fourier transform of a circular disc which can be expressed in terms of $J_1(2\pi U\theta_\nu)$, the first order Bessel function (Paper I). In each channel, the signal has a peak value $|S(0, \nu)| = \pi x_{\text{HI}} \bar{I}_\nu \theta_\nu^2$ where $\bar{I}_\nu = 2.5 \times 10^2 \frac{J_{\text{HI}}}{\text{sr}} \left(\frac{\Omega_b h^2}{0.02} \right) \left(\frac{0.7}{h} \right) \left(\frac{H_0}{H(z)} \right)$ is the background HI specific intensity expected from completely neutral medium. The signal is largely contained within baselines $U \leq U_0 = 0.61/\theta_\nu$ where the Bessel function has its first zero crossing, and the signal is much smaller at larger baselines. The signal $S(\vec{U}, \nu)$ picks up an extra phase if the bubble is shifted from the center of the FoV. The amplitude of the signal also falls because of the telescope's primary

beam pattern (Paper I), and in this paper we restrict our analysis to the most favourable situation where the bubble is at the center of the FoV. The terms x_{HI} , \bar{I}_ν , θ_ν and $\Delta\nu_b$ are all redshift dependent, and hence the signal too is strongly redshift dependent. In Section 3 we will discuss the combined effect of all these factors on bubble detection.

In order to detect an ionized bubble whose expected signal is $S(\vec{U}, \nu)$ we use the matched filter $S_f(\vec{U}, \nu)$ defined as

$$S_f(\vec{U}, \nu) = \left(\frac{\nu}{\nu_c} \right)^2 \left[S(\vec{U}, \nu) - \Theta \left(1 - 2 \frac{|\nu - \nu_c|}{B'} \right) \frac{1}{B'} \int_{\nu_c - B'/2}^{\nu_c + B'/2} S(\vec{U}, \nu') d\nu' \right]. \quad (2)$$

Note that the filter is constructed using the signal that we are trying to detect. The term $(\nu/\nu_c)^2$ accounts the frequency dependent U distribution for a given array. The function Θ is the Heaviside step function. The second term in the square brackets serves to remove the foregrounds within the frequency range $\nu_c - B'/2$ to $\nu_c + B'/2$. Here $B' = 4 \Delta\nu_b$ is the frequency width that we use to estimate and subtract out a frequency independent foreground contribution. This, we have seen in Paper I, is adequate to remove the foregrounds such that the residuals are considerably smaller than the signal. Further we have assumed that B' is smaller than the total observational bandwidth B . The filter $S_f(\vec{U}, \nu)$ depends on $[R_b, z_c, \vec{\theta}_c]$ the comoving radius, redshift and angular position of the target bubble that we are trying to detect.

Bubble detection is carried out by combining the entire observed visibility signal weighed with the filter. The estimator \hat{E} is defined as

$$\hat{E} = \left[\sum_{a,b} S_f^*(\vec{U}_a, \nu_b) \hat{V}(\vec{U}_a, \nu_b) \right] / \left[\sum_{a,b} 1 \right], \quad (3)$$

where the sum is over all frequency channels and baselines. The expectation value $\langle \hat{E} \rangle$ is non-zero only if an ionized bubble is present, and it is zero if there is no bubble in the FoV.

The system noise (NS), HI fluctuations (HF) and the foregrounds (FG) all contribute to the variance of the estimator

$$\langle (\Delta \hat{E})^2 \rangle = \langle (\Delta \hat{E})^2 \rangle_{\text{NS}} + \langle (\Delta \hat{E})^2 \rangle_{\text{HF}} + \langle (\Delta \hat{E})^2 \rangle_{\text{FG}} \quad (4)$$

A 3σ detection is possible only if $\langle \hat{E} \rangle > 3\sqrt{\langle (\Delta \hat{E})^2 \rangle}$. In a situation where this condition is satisfied, the observed value E_0 may be interpreted as a detection if $E_0 > 3\sqrt{\langle (\Delta \hat{E})^2 \rangle}$.

Because of our choice of the matched filter, the contribution from the residuals after foreground subtraction $\langle (\Delta \hat{E})^2 \rangle_{\text{FG}}$ is predicted to be smaller than the signal (Paper I) and we do not consider it in the subsequent analysis. The contribution $\langle (\Delta \hat{E})^2 \rangle_{\text{HF}}$ which arises from the HI fluctuations outside the target bubble imposes a fundamental restriction on bubble detection. It is not possible to detect an ionized bubbles for which $\langle \hat{E} \rangle \lesssim \sqrt{\langle (\Delta \hat{E})^2 \rangle_{\text{HF}}}$. Bubble detection is meaningful only in situations where the contribution from HI fluctuations is considerably smaller than the expected signal. Once this condition is satisfied, it is the SNR defined as

$$\text{SNR} = \langle \hat{E} \rangle / \sqrt{\langle (\Delta \hat{E})^2 \rangle_{\text{NS}}} \quad (5)$$

which is important for bubble detection. The value of SNR peaks

when the parameters of the filter exactly match the bubble that is actually present in the observation, and decreases from its peak value if there is a mis-match (Paper II). In the subsequent analysis we shall use this to assess the redshift that is optimal for bubble detection.

It is possible to analytically estimate $\langle \hat{E} \rangle$, $\langle (\Delta \hat{E})^2 \rangle_{\text{NS}}$ and $\langle (\Delta \hat{E})^2 \rangle_{\text{HF}}$ in the continuum limit (Paper I). We have

$$\langle \hat{E} \rangle = \int d^2U \int d\nu \rho_N(\vec{U}, \nu) S_f^*(\vec{U}, \nu) S(\vec{U}, \nu), \quad (6)$$

$$\langle (\Delta \hat{E})^2 \rangle_{\text{NS}} = \sigma^2 \int d^2U \int d\nu \rho_N(\vec{U}, \nu) |S_f(\vec{U}, \nu)|^2. \quad (7)$$

and

$$\begin{aligned} \langle (\Delta \hat{E})^2 \rangle_{\text{HF}} &= \int d^2U \int d\nu_1 \int d\nu_2 \left(\frac{dB_{\nu_1}}{dT} \right) \left(\frac{dB_{\nu_2}}{dT} \right) \\ &\quad \times \rho_N(\vec{U}, \nu_1) \rho_N(\vec{U}, \nu_2) S_f^*(\vec{U}, \nu_1) S_f(\vec{U}, \nu_2) \\ &\quad \times C_{2\pi U}(\nu_1, \nu_2) \end{aligned} \quad (8)$$

where B_ν is the specific intensity of blackbody radiation (which can be approximated as $2k_B T \nu^2 / c^2$ in the Rayleigh-Jeans regime) and $\rho_N(\vec{U}, \nu)$ is the normalized baseline distribution function defined so that $\int d^2U \int d\nu \rho_N(\vec{U}, \nu) = 1$. For a given observation, $d^2U d\nu \rho_N(\vec{U}, \nu)$ is the fraction of visibilities in the interval $d^2U d\nu$ of baselines and frequency channels. Further, we expect $\rho_N(\vec{U}, \nu) \propto \nu^{-2}$ for an uniform distribution of the antenna separations \mathbf{d} .

The term σ in eq. (7) is the rms. noise expected in an image made using the radio-interferometric observation being analyzed. Assuming observations at two polarizations, we have

$$\sigma = \frac{k_B T_{sys}}{A_{eff} \sqrt{N_b t_{obs} B}} \quad (9)$$

where k_B is the Boltzmann constant, T_{sys} the system temperature, A_{eff} the effective collecting area of an individual antenna in the array, N_b the number of baselines, t_{obs} the total observing time and B the observing bandwidth.

The contribution from HI fluctuations $\langle (\Delta \hat{E})^2 \rangle_{\text{HF}}$ is calculated using $(\frac{dB_\nu}{dT})$, the conversion factor from temperature to specific intensity at frequency ν , and $C_{2\pi U}(\nu_1, \nu_2)$ the multi-frequency angular power spectrum (MAPS; (Datta, Choudhury & Bharadwaj 2007)). The HI distribution during the epoch of reionization is highly uncertain. The value of $\langle (\Delta \hat{E})^2 \rangle_{\text{HF}}$ is sensitive to the size and clustering of the ionized patches outside the target bubble (Paper II). Given the lack of information, we make the simplifying assumption that the HI outside the target bubble exactly traces the dark matter. This gives the most optimistic constraints on bubble detection, the constraints are more severe if patchy reionization is included.

3 SCALING RELATIONS

The scaling of the expectation value of the estimator with various parameters can be estimated from eq. (6) whereby

$$\langle \hat{E} \rangle \propto U_0^2 \Delta \nu_b \nu_c^{-2} |S(0, \nu_c)|^2. \quad (10)$$

Here we have assumed that B' is larger than the frequency extent of the bubble $\Delta \nu_b$ and that the baselines in the array extend well beyond U_0 . Further it is assumed that the array configuration is such that the antenna separations \mathbf{d} are uniformly sampled, whereby $\rho(\vec{U}, \nu) \propto \nu^{-2}$. Considering the noise contribution next, it also

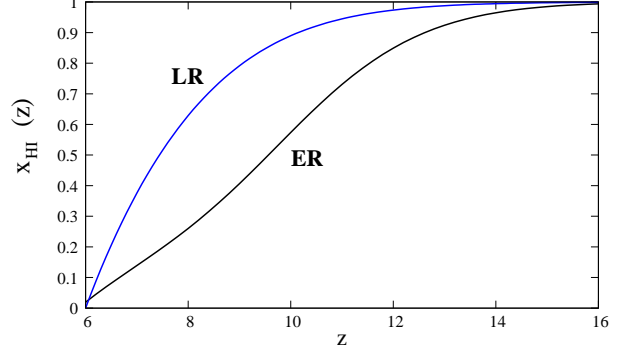


Figure 1. The evolution of the mean neutral fraction x_{HI} with redshift for the two different reionization models discussed in the text.

follows from eq.(7) that $\langle (\Delta \hat{E})^2 \rangle \propto \sigma^2 \langle \hat{E} \rangle$. We use these and the relations from the previous Section to determine that the SNR scales as

$$\text{SNR} \propto A_{eff} \sqrt{N_b t_{obs}} \frac{1}{T_{sys}} x_{\text{HI}} \sqrt{\frac{R_b^3}{r_\nu^2 r'_\nu} \frac{(1+z_c)}{H(z_c)}}. \quad (11)$$

This completely quantifies the dependence on the telescope parameters, observation time, system temperature, neutral fraction, bubble radius and the background expansion history. In principle, measurements of the SNR will provide a unique and independent way to probe the source properties (through R_b ; (Yu 2005)), intergalactic medium, and the background cosmology during the EoR. For the redshift range of our interest it is reasonable to assume $r_\nu \propto (1+z)^{0.25}$, $r'_\nu \propto (1+z)^{0.5}$ and $H(z) \propto (1+z)^{1.5}$. Further, for the frequency range of our interest the system temperature is dominated by the sky temperature which scales as $T_{\text{sky}} \propto \nu^{-\beta}$ with $\beta \sim 2.6$ which implies $T_{sys} \propto (1+z)^\beta$. The effective collecting area is nearly constant for dish antennas like the GMRT whereas it scales as $A_{eff} \propto \nu^{-2}$ for dipoles (eg. MWA). Combining all of these factors we determine the scaling of the SNR with redshift

$$\text{SNR} \propto x_{\text{HI}}(z) (1+z)^\alpha \quad (12)$$

where $\alpha = -\beta - 1$ or $\alpha = -\beta + 1$ for dish antennas or dipoles respectively. While x_{HI} increases with z , the other term $(1+z)^\alpha$ has the opposite behaviour. These two competing effects decide the redshift where the SNR peaks which is the optimal redshift for bubble detection.

The baseline distribution, in general, does not uniformly sample all baselines. Typically, the sampling falls at larger baselines and we do not expect the scaling relations discussed here to be exactly valid. The deviations from the scaling relations depend on the bubble size and the array configuration, and in the next Section we discuss these for the GMRT and the MWA.

3.1 Evolution of neutral fraction with redshift

In this work, we consider two physically motivated models of reionization, namely, the early reionization (ER) and the late reionization (LR) scenario. These models are constructed using the semi-analytical formalism (Choudhury & Ferrara 2005; Choudhury & Ferrara 2006a) which implements most of the relevant physics governing the thermal and ionization history of the IGM, such as the inhomogeneous IGM density distribution, three different classes of ionizing photon sources (massive Pop III stars, Pop II stars and QSOs), radiative feedback inhibiting star formation in low-mass galaxies and chemical feedback for transition from Pop

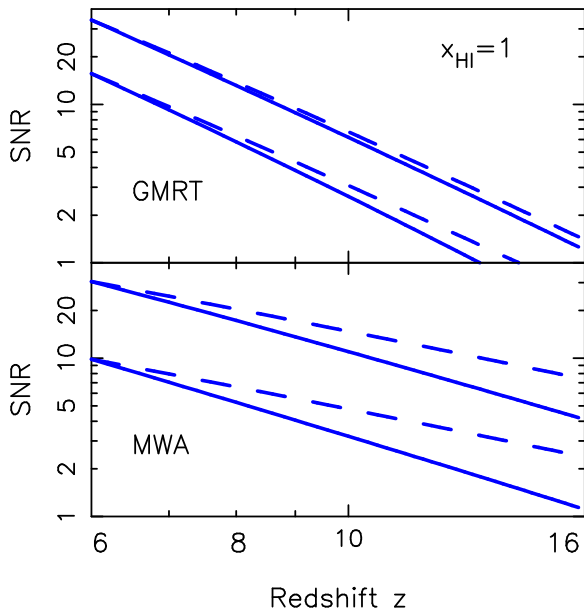


Figure 2. Assuming $x_{\text{HI}} = 1$, the dashed lines show the predicted scaling of the SNR for uniform baseline coverage (eq. 12), the solid lines are calculated numerically incorporating non-uniform baseline coverage. For both GMRT (upper panel) and MWA (lower panel), the upper curves are for $R_b = 50$ Mpc with 1000 hrs observation, and the lower curves for $R_b = 20$ Mpc with 4000 hrs.

III to Pop II stars. The models are consistent with various observational data, namely, the redshift evolution of Lyman-limit absorption systems (Storrie-Lombardi et al. 1994), the Gunn-Peterson effect (Songaila 2004), electron scattering optical depths (Kogut et al. 2003), temperature of the IGM (Schaye et al. 1999) and cosmic star formation history (Nagamine et al. 2005). We assume that these two models “bracket” the range of models which are consistent with available data.

In ER scenario, hydrogen reionization starts around $z \approx 16$ driven by metal-free (Pop III) stars, and it is 50% complete by $z \approx 10$. The contribution of Pop III stars decrease below this redshift because of the combined action of radiative and chemical feedback. As a result, reionization is extended considerably completing only at $z \approx 6$ (Figure 1). In LR scenario, the contribution from the metal-free stars is ignored, which makes reionization start much later and is only 50% complete only around $z \approx 7.5$. The main difference between the ER and LR models is in their predictions for the electron scattering optical depth (which is 0.12 and 0.06 for the ER and LR scenarios, respectively).

4 RESULTS AND CONCLUSIONS

We consider two possible definitions of the ‘optimal redshift’ for bubble detection. The first is the redshift where, for a fixed observing time and bubble radius R_b , the SNR is maximum. Another possibility is, for a fixed observing time and SNR, the redshift where a bubble of the smallest size can be detected. While the two definitions are the same if the instrument has uniform baseline coverage, we do not expect this to be true in general.

We have used equations (6), (7) and (8) to calculate the SNR and determine the constraints from HI fluctuations. The baseline distribution function $\rho_N(\vec{U}, \nu)$, which we assume to be circularly symmetric ($\rho_N(\vec{U}, \nu) = \rho_N(U, \nu)$), has been calculated in Paper I for both the GMRT and the MWA. In both cases $\rho_N(U, \nu)$ falls off

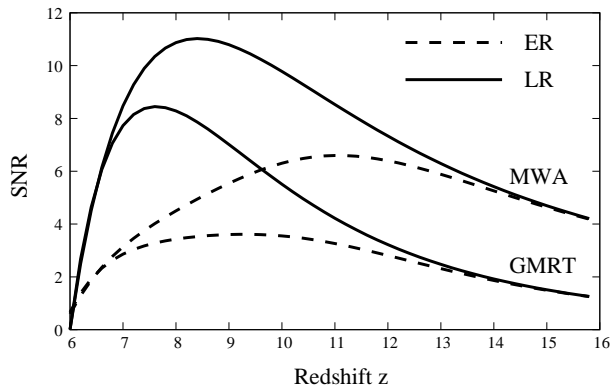


Figure 3. The SNR for $R_b = 50$ Mpc and 1000 hrs observation. Results are shown for both GMRT and MWA using the two different reionization models (ER and LR) discussed in the text.

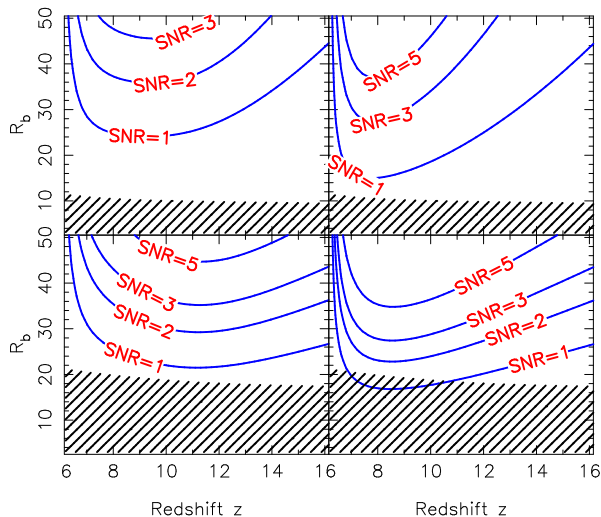


Figure 4. SNR contours as a function of the redshift z and comoving bubble radius R_b , considering 1000 hrs of observation with the GMRT (upper panels) and MWA (lower). The left and right panels show the ER and the LR scenarios respectively. The shaded region is ruled out due to the HI fluctuations.

with increasing U . For the GMRT $\rho_N(U, \nu)$ is roughly constant for antenna separations $d < 1$ km and it extends out to large baselines $d \sim 25$ km. For the MWA we have assumed that the antennas are distributed over a circular region of diameter 1.5 km, with the number density of antennas falling as $1/r^2$ with the distance from the center.

We first consider, for a fixed bubble radius and observing time, how the SNR varies with z . Assuming $x_{\text{HI}} = 1$ and uniform baseline coverage, we expect that $\text{SNR} \propto (1+z)^\alpha$ with $\alpha = -3.6$ and -1.6 for GMRT and MWA respectively. For the GMRT, we find (Figure 2) that the predicted scaling holds for large bubbles $R_b \geq 50$ Mpc where the entire signal lies within a small baseline range which is nearly uniformly sampled. For smaller bubbles a significant amount of signal spreads over to larger baselines which are not uniformly sampled. We find that α changes, approximately linearly, from -3.6 to -4.1 as R_b is varied from 50 to 20 Mpc. For the MWA, the non-uniform baseline coverage makes the scaling steeper than -1.6 for all values of R_b , and we find $\alpha = -2.4$ and -2.5 for $R_b = 50$ and 20 Mpc respectively. We combine these findings with earlier results at $z = 8.3$ (Paper I) as to how the SNR

Table 1. Dimensionless parameters required to calculate the SNR using eq. (13). The values of R_b are restricted to the range $50 \text{ Mpc} \geq R_b \geq 20 \text{ Mpc}$.

	K	α	γ
GMRT	9.1	$-3.6 - \left(50 - \frac{R_b}{\text{Mpc}}\right) / 60$	1.5
MWA	13.4	-2.4	2.0

Table 2. For $R_b = 50 \text{ Mpc}$ and 1000 hrs of observation, the optimal redshift z_o where the SNR peaks, the peak value and the z range where the SNR is within 80 % of the peak value.

		z_o	Peak SNR	80 % z range
GMRT	ER	9.2	3.6	7 - 12
	LR	7.6	8.4	6.8 - 9.2
MWA	ER	11.0	6.59	8.8 - 14
	LR	8.4	11	7.1 - 10.8

scales with R_b to obtain

$$\text{SNR} = x_{\text{HI}} K \left(\frac{t}{1000 \text{ hrs}} \right)^{0.5} \left(\frac{1+z}{10} \right)^\alpha \left(\frac{R_b}{50 \text{ Mpc}} \right)^\gamma \quad (13)$$

where t is the observing time, and α , γ and K are parameters whose values are listed in Table 1. This expression is found to match the numerically computed SNR to within 20%, which is quite adequate given the large uncertainty in x_{HI} .

Considering Figure 3 which shows the SNR for the two reionization models, we find that it increases monotonically as z decreases when $x_{\text{HI}} \approx 1$ and thereafter declines rapidly once $x_{\text{HI}} \leq 0.5$. The peak SNR, the corresponding optimal redshift z_o and the z range where the SNR is within 80 % of the peak value are tabulated in Table 2. Results have been shown only for $R_b = 50 \text{ Mpc}$ and $t = 1000 \text{ hrs}$ of observation, these can be easily scaled to other R_b and t values using eq. (13). The z dependence is not very different for smaller bubbles in the range $50 > R_b \geq 20 \text{ Mpc}$.

The effective collecting area of the individual MWA antennas increases with wavelength as λ^2 . This reduces the noise at higher redshifts, and puts the MWA at an advantage over the GMRT in detecting bubbles at high redshifts. This also pushes the optimal redshift for MWA to a higher value as compared to the GMRT (Table 2). The MWA is also at an advantage over the GMRT in detecting large bubbles ($R_b \sim 50 \text{ Mpc}$, Figure 3). The SNR scales differently with R_b for the two instruments (Table 1), and the advantage that the MWA has for large bubbles balances out as the bubble size is reduced. GMRT and MWA have nearly comparable SNR for $R_b = 30 \text{ Mpc}$.

We next consider the other definition of the optimal redshift where for a fixed observing time and SNR, we determine z_o where a bubble of the smallest size can be detected. Considering the constant SNR contours in Figure 4, we find that the z_o values are roughly consistent with those in Table 2. This shows that for both the GMRT and the MWA, for $50 > R_b \geq 20 \text{ Mpc}$ the two definitions predict the same optimal redshift which is approximately independent of the bubble size. We do not expect this to hold for smaller bubbles $R_b \sim 10 \text{ Mpc}$ where a detection is possible only with the GMRT, the signal being smaller than the HI fluctuations in the MWA (Paper I).

Given the lack of knowledge about the reionization history, it would be most judicious to choose a redshift where a high SNR is predicted for both the ER and LR models. We find that the redshift range 7 – 9.2 and 8.8 – 10.8 are most appropriate for the GMRT and MWA respectively. For both instruments, the prospects of a detection are considerably improved in the late reionization scenario. Assuming 1000 hrs of observation, in the ER and LR models respectively, a 3σ detection is possible with the GMRT for $R_b \sim 50$ and 30 Mpc or larger. The same figures are 40 and 30 Mpc for the MWA.

The actual distribution of bubble sizes is an important issue for bubble detection. This depends on the reionization history and the distribution of ionizing sources which are largely unknown. We generally expect a predominance of larger bubbles at lower redshifts. Analytic estimates (Furlanetto et al. 2006; Rhook & Haehnelt 2006) do not rule out bubbles in the parameter range amenable for detection with the GMRT and MWA.

In conclusion, we find that the optimal redshift for bubble detection is determined by a combination of instrument dependent factors and the evolution of the neutral fraction x_{HI} . We propose that the redshift 8.1 ± 1.1 and 9.8 ± 1 are optimum for detecting ionized bubbles with the GMRT and MWA respectively. The prospects of a detection are most favourable for late reionization with $x_{\text{HI}} \sim 0.5$ at $z \sim 8$ where for both instruments a 3σ detection is possible for $R_b \geq 30 \text{ Mpc}$ with 1000 hrs of observation. Future observations will either lead to the detection of ionized bubbles, or lead to constraints on the product $x_{\text{HI}} R_b^\gamma$ for the observational volume in the event of non-detection.

5 ACKNOWLEDGMENT

KKD would like to thank CSIR, India for financial support.

REFERENCES

- Ali, S. S., Bharadwaj, S., & Chengalur, J. N. 2008, MNRAS, 385, 2166
 Bowman, J. D., et al. 2007, AJ, 133, 1505
 Choudhury, T. R., & Ferrara, A. 2005, MNRAS, 361, 577
 Choudhury, T. R., Ferrara, A., 2006, Cosmic Polarization, Ed. R. Fabbri (Research Signpost), p. 205, arXiv:astro-ph/0603149
 Choudhury, T. R., & Ferrara, A., 2006a, MNRAS, 371, L55
 Datta, K. K., Choudhury, T. R., & Bharadwaj, S. 2007, MNRAS, 378, 119
 Datta, K. K., Bharadwaj, S., & Choudhury, T. R., 2007, MNRAS, 382, 809 (Paper I)
 Datta, K. K., Majumdar, S., Bharadwaj, S., & Choudhury, T. R. 2008, MNRAS, 391, 1900
 Dunkley, J., et al. 2009, ApJS, 180, 306
 Fan, X., et al. 2006, AJ, 132, 117
 Furlanetto, S. R., McQuinn, M., & Hernquist, L. 2006, MNRAS, 365, 115
 Geil, P. M., & Wyithe, J. S. B. 2008, MNRAS, 386, 1683
 Kogut, A., et al. 2003, ApJS, 148, 161
 Komatsu, E., et al. 2009, ApJS, 180, 330
 Maselli, A., Gallerani, S., Ferrara, A. & Choudhury, T. R. 2007, MNRAS, 376, L34
 Nagamine, K., Cen, R., Hernquist, L., Ostriker, J. P., & Springel, V. 2005, ApJ, 618, 23
 Rhook, K. J., & Haehnelt, M. G. 2006, MNRAS, 373, 623
 Schaye, J., Theuns, T., Leonard, A., & Efstathiou, G. 1999, MNRAS, 310, 57
 Songaila, A. 2004, AJ, 127, 2598
 Wyithe, J. S. B., & Loeb, A. 2004, ApJ, 610, 117
 Wyithe, J. S. B., Loeb, A., & Barnes, D. G. 2005, ApJ, 634, 715
 Yu, Q. 2005, ApJ, 623, 683